first site at which Fe binds on the path to oxidation and mineralization. The heterogeneity of the Fe(III)-tyrosinate ν_{V-O} Raman modes could arise from different conformers involving Fe(III)-Tyr^{25}. Alternatively, Tyr^{25} and another nearby Tyr, such as Tyr^{28} or Tyr^{30}, might both be involved. Multiple ν_{C-O} Raman modes have been observed for protocatechuate 3,4-dioxygenase, which has two Tyr ligands per Fe (*15, 16*). Finally, an additional Fe(III)-Tyr moiety could cause heterogeneity in the Raman spectrum. Such a site could be Tyr^{133}, which, although conserved in all known vertebrate H-subunit ferritins, is also in mouse L (*17*) and bullfrog red cell L (*9*) ferritin. It is close to the Tb^{+3}-binding "ferroxidase" site in human H-subunit ferritin (*14*). Involvement of Tyr^{133} would require an environment unique to the H subunit because the L subunit does not form detectable amounts of the Fe(III)-Tyr complex (*18*).

The Fe(III)-Tyr complex appears to be a transient precursor of polynuclear cluster formation. Such a notion is supported by the observation that smaller numbers of Fe atoms per ferritin formed Fe(III)-Tyr complexes with greater stability and a larger fraction of monomeric Fe(III) (*19*). On the basis of quantitation of the $g' = 4.3$ signal in the electron paramagnetic resonance (EPR) spectrum (*19*), ferritin with 24 Fe atoms per molecule contained 20 ± 4% monomeric Fe(III). If all the monomeric Fe was present as Fe(III)-Tyr, the molar extinction coefficient, $\epsilon_{550\ nm}$, is 1800 ± 400 M^{-1} on a per-metal basis, which is within the range found for Fe(III)-Tyr proteins (1200 to 4000 M^{-1}) (*20*). Finally, x-ray absorption near-edge structure (XANES) spectroscopy (*19*) showed that all of the Fe was present as Fe(III); therefore, the EPR-silent Fe is likely to be multimeric Fe(III).

Tyrosine as a ligand for Fe in ferritin has been little discussed. Previously, attention had been focused either on Glu residues conserved in all subunit types or on the Glu^{58} and His^{61} residues, which have been considered to be H-subunit specific, at least in mammals (*2, 7, 8, 10*). The presence of the Glu^{58} and His^{61} residues in bullfrog red cell L-subunit ferritin demonstrates their lack of subunit specificity. Clearly, these residues alone are not sufficient to confer a rapid rate of mineralization on the protein (Figs. 1B and 2). The H subunit–specific Fe(III)-Tyr species (Fig. 3A) may be a key to understanding the differences in the mineralization rate of ferritin protein formed from H or L subunits.

REFERENCES AND NOTES

1. E C Theil, *Adv. Enzymol Relat Areas Mol. Biol* **63**, 421 (1990).
2. P. M. Harrison and T. H Lilley, in *Iron Carriers and Iron Proteins*, T. M. Loehr, Ed. (VCH, New York, 1989), pp 123–238.
3. M J Grossman *et al*, *Proc. Natl Acad Sci. U S.A.* **89**, 2419 (1992)
4. M. Ragland *et al.*, *J. Biol. Chem.* **265**, 18339 (1990)
5. C Y. Yang *et al.*, *Biochemistry* **26**, 497 (1987).
6. E Bauminger, P M. Harrison, I Nowik, A Treffrey, *ibid.* **28**, 5486 (1989)
7. P M. Hanna, N D. Chasteen, G. A. Rottman, P. Aisen, *ibid.* **30**, 9210 (1991).
8. D M Lawson *et al.*, *Nature* **349**, 541 (1991).
9. L. F. Dickey *et al.*, *J Biol. Chem.* **262**, 7901 (1987).
10. V J. Wade *et al.*, *J. Mol Biol* **221**, 1443 (1991)
11. M. J. Yablonski and E C Theil, *Biochemistry* **31**, 9680 (1992)
12. L. Que, Jr , in (*2*), pp 457–524.
13. ———, in *Biological Applications of Raman Spectroscopy*, T G. Spiro, Ed. (Wiley, New York, 1988), vol. 3, pp 491–521
14. R. W. Rice, G. C Ford, J. L. White, J. M. A. Smith, P. M. Harrison, *Adv. Inorg. Biochem.* **5**, 39 (1983).
15. D. H. Ohlendorf, J. D Lipscomb, P C. Weber, *Nature* **336**, 403 (1988).
16. L. Que, Jr., and R M. Epstein, *Biochemistry* **20**, 2545 (1981).
17. C. Beaumont *et al.*, *J. Biol. Chem.* **264**, 7498 (1989).
18. The purple Fe(III)-Tyr complex was not observed in the L subunit, even though Tyr^{133} is present However, it could have formed in amounts undetectable if its concentration was low as a result of rapid conversion to Fe(III) bound to other residues. Alternatively, Fe(III)-Tyr may not form in L-subunit ferritin, which may be related to the low rate of mineralization (Fig. 1B).
19. After maximum formation of the 550-nm absorbance, samples were rapidly transferred to Ar-purged quartz EPR tubes and frozen in liquid nitrogen. We measured x-band EPR spectra with a JEOL-JES RE-1X spectrometer equipped with a TE011 cylindrical cavity operated at 100 K, 1-mW microwave power, 9.20-GHz microwave frequency, and 1-mT modulation. The fraction of monomeric Fe(III) in each sample was determined by double integration of the $g' = 4.3$ signal from 110 to 220 mT, relative to a 1 mM Fe nitrilotriacetic acid standard in 50% glycerin, pH = 4.5. Spectra from XANES (x-ray absorption near edge structure) spectroscopy were measured at 77 K in collaboration with D. E. Sayers on beamline X11-A at the National Synchrotron Light Source. We quantified Fe(II) and Fe(III) by fitting with linear combinations of model compounds as in (*21*).
20. L Que, Jr., *Coord. Chem. Rev.* **50**, 73 (1983).
21. M.-S. Joo, G. Tourillon, D. E Sayers, E. C. Theil, *Biol. Met.* **3**, 171 (1990).
22. F. W. Studier, A. H. Rosenberg, J. J. Dunn, J. S. Dubendorff, *Methods Enzymol.* **185**, 60 (1990).
23. M Heusterspreute and R. R Crichton, *FEBS Lett.* **129**, 322 (1981).
24. D. Boyd *et al.*, *J. Biol Chem.* **260**, 11755 (1985).
25. E. A Leibold and H. N. Munro, *ibid.* **262**, 7335 (1987)
26. S. Daniels-McQueen *et al.*, *Nucleic Acids Res* **16**, 7741 (1988).
27. M. J. Murray, K. White, H. N. Munro, *Proc. Natl. Acad. Sci. U.S.A.* **84**, 7438 (1987).
28. P. W. Stevens, J. B. Dodgson, J. D. Engel, *Mol. Cell. Biol.* **7**, 1751 (1987).
29. Abbreviations for the amino acid residues are: A, Ala; C, Cys; D, Asp; E, Glu; F, Phe; G, Gly; H, His; I, Ile; K, Lys; L, Leu; M, Met; N, Asn; P, Pro; Q, Gln; R, Arg; S, Ser; T, Thr; V, Val; W, Trp; and Y, Tyr.
30. T. M. Loehr and J. Sanders-Loehr, *Methods Enzymol.*, in press.
31. B. A. Averill *et al.*, *J. Am Chem. Soc.* **109**, 3760 (1987).
32. J. W. Pyrz, A. L. Roe, L. J. Stern, L. Que, Jr., *ibid.* **107**, 614 (1985).

33. We thank D. Stout and S. Sreedharan for engineering the ferritin proteins, M. Forbes for use of the JEOL-JES RE-1X EPR spectrometer, and P. Aisen for helpful discussions on spin quantitation. Support by NIH grants DK-20251 (G.S.W. and E.C T.) and GM-18865 (J.S.-L.).

7 August 1992, accepted 9 November 1992

Molecular Positional Order in Langmuir-Blodgett Films by Atomic Force Microscopy

L. Bourdieu, O. Ronsin, D. Chatenay

Langmuir-Blodgett films of barium arachidate have been studied on both macroscopic and microscopic scales by atomic force microscopy. As prepared, the films exhibit a disordered hexagonal structure; molecularly resolved images in direct space establish a connection between the extent of the positional order and the presence of defects such as dislocations. Upon heating, the films reorganize into a more condensed state with a centered rectangular crystallographic arrangement; in this new state the films exhibit long-range positional order and unusual structural features, such as a height modulation of the arachidic acid molecules.

Langmuir-Blodgett (LB) films (*1*) have attracted much attention because of their potential use in molecular electronics (*2*), integrated optics (*3*), and the development of biological sensors (*4*); in addition to these practical applications, LB films are also used as model systems for certain aspects of two-dimensional (2-D) physics such as the description of 2-D solids and the existence of hexatic phases. For practical applications, one must consider the structure and thermal behavior of the films on both macroscopic and microscopic scales; from a fundamental point of view it has not yet been possible to establish a link between the extent of the positional order in these systems and the presence of defects at the molecular level. For these investigations, atomic force microscopy (AFM) has recently been shown to be a powerful tool (*5–9*). In contrast to other techniques such as x-ray (*10–12*) and electron (*13–15*) diffrac-

Institut Curie, Section de Physique et Chimie, Laboratoire de Physico-Chimie des Surfaces et Interfaces, Unité Associée CNRS 1379, 11 rue Pierre et Marie Curie, 75005 Paris, France.

tion, which measure an "average" structure, AFM allows one to observe the structure in real space and to visualize local defects such as pairs of dislocations (5, 9).

We report here on the use of AFM to observe the microscopic positional order of a bilayer of barium arachidate; the extent of this order is found to be about ten molecular spacings. Direct space imaging of the molecular organization shows that this rather short-range positional order originates from the presence of dislocations. Subsequently, we investigated the evolution of both macroscopic and microscopic structures of the bilayer upon annealing. At macroscopic scales, the annealing causes dewetting of the bilayer, leading to the formation of multilayered structures coexisting with patches of the bilayer, in which we observe an unusual crystallographic arrangement and a 13% decrease of the area per molecule. At the same time, the extent of the positional order increases dramatically. Finally, a buckling phenomenon is observed.

The LB films were prepared in a clean, temperature-controlled room according to the following procedure. We first deposited arachidic acid (AA) at room temperature (20°C) on water at pH = 5.5, 6.5, or 9 in the presence of 10^{-4} M $BaCl_2$ and compressed the monolayer into its solid phase at a surface pressure of 30 mN/m; in this phase each AA molecule occupies an area of 20 ± 0.5 Å^2. We transferred two solid layers onto a silanated silicon wafer (16), so that we could observe the organization of the aliphatic chains. The silane molecules on the silicon wafer have only short-range, liquid-like positional order (17). Transfers were controlled by measurements of the area variations of the monolayer and by optical observations (5).

In the AFM experiments we used a Nanoscope II microscope (Digital Instruments). For all the images presented here, forces were of the order of 10^{-8} N. Images are gray scale–encoded (dark regions are deeper than the lighter ones). The large-scale images were obtained with the microscope feedback loop, which moves the samples up and down, in order to maintain at a constant value the force applied by the tip on the sample. Height measurements were deduced from the vertical displacements of

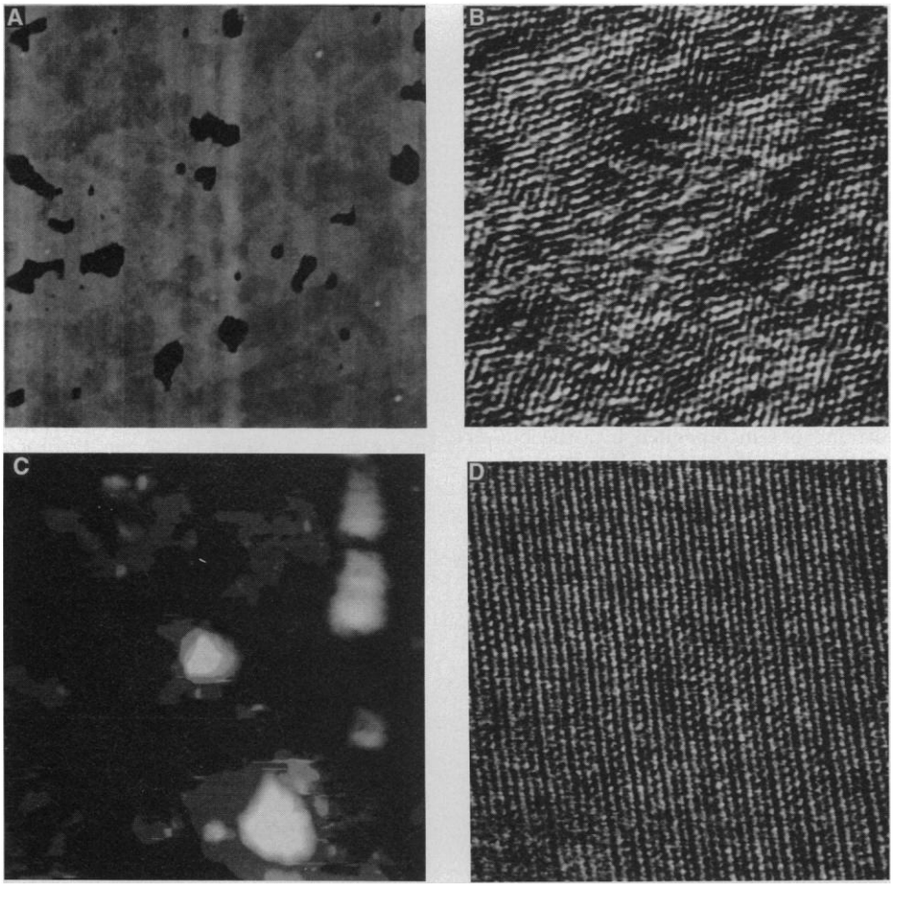

Fig. 1. AFM images of a barium arachidate bilayer before and after annealing. (**A**) Large-scale image (1.7 μm by 1.7 μm) of the LB film prepared and observed at 20°C. Holes with a depth of 5.4 nm and about 200 nm in lateral extension are clearly visible within the bilayer. (**B**) Molecular scale image (20 nm by 20 nm) of the bilayer obtained by averaging six images. The addition procedure allows the observation of a high density of dislocations without any filtering. (**C**) Large-scale image (1.7 μm by 1.7 μm) of a bilayer after annealing at 80°C. This image shows various types of domains coexisting with remaining patches of the bilayer. (**D**) Molecular scale image (20 nm by 20 nm) of the annealed bilayer obtained by averaging six images. Such a structure can be observed on any layered domain of the image shown in (C). The extent of the positional order is much greater than in (B). In one direction, one molecular row out of three is a bit higher than the other two. From images obtained with the feedback loop of the microscope, we measured the height difference to be about 0.2 Å. One also sees a slight modulation of rows spacings. This buckling was never observed before annealing.

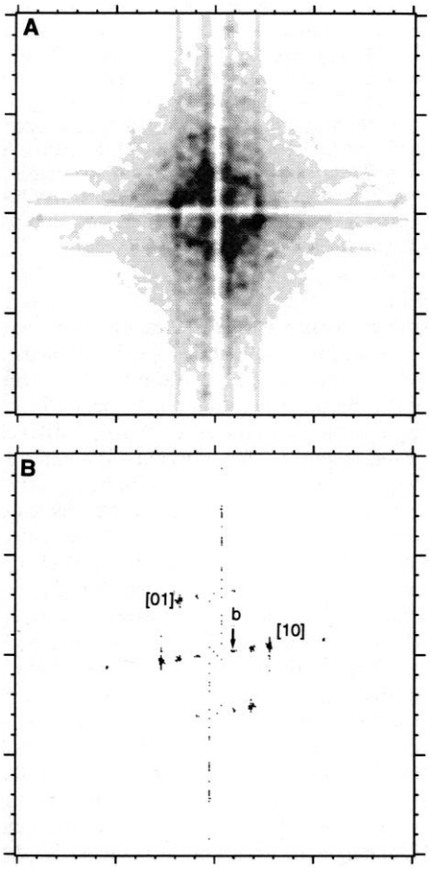

Fig. 2. Two-dimensional Fourier transform of the LB film, showing the molecular organization before and after annealing. (**A**) Hexagonal structure of unannealed samples. The structure was deduced from an examination of 20 such images obtained with different tips and with different orientations of the tips with respect to the crystallographic axes of the samples. One pair of spots is much weaker than the two others; this originates from the anisotropic tip. (**B**) Centered rectangular structure of annealed samples. The [10] and [01] spots of the lattice elementary basis are displayed. The spot labeled "b" corresponds to the buckling observed in real space; its spatial frequency is equal to one-third of the [10] spot frequency.

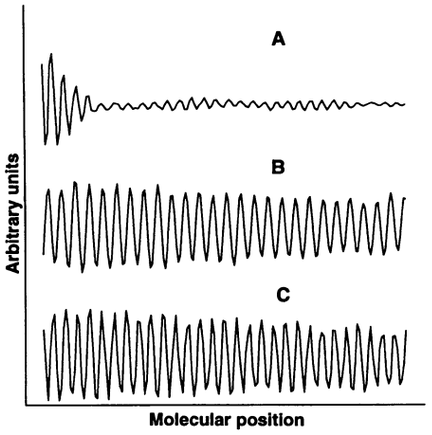

Fig. 3. Cross sections of the 2-D autocorrelation functions calculated from images of mica (curve C) (shown as a reference), unannealed LB films (curve A), and annealed LB films (curve B), containing the same number of molecules. These scans were performed along the crystallographic axes. Each oscillation represents one intermolecular spacing. In curves B and C, the slight decrease of the autocorrelation function is the result of the finite size of the images. Unannealed LB films are less ordered than annealed ones.

the piezoelectric (PZT) scanner and were measured from height histograms of images. Most of the images at the molecular scale were obtained without the feedback loop, by optical measurements of the cantilever displacements. This procedure allows faster scans of the samples, thus minimizing drifts while imaging. In order to further decrease those drifts, PZT scanners were activated overnight before imaging. We further improved image quality by averaging six images from six successive downward scans of the same location of the sample. We took small residual drifts into account, before averaging, by computing the maximum of the cross-correlation function of two successive images in order to determine their spatial shift. Averaging was then performed with shifted images. The whole procedure, as well as the Fourier analysis, was performed, with the raw data files of the Nanoscope II, on a microcomputer. This procedure was a very efficient and general way to improve AFM images without any filtering.

We first studied the films prepared at pH = 6.5 at 20°C. The large-scale image (Fig. 1A) shows isolated holes with typical lateral sizes between 100 to 400 nm. Their depth was 5.4 ± 0.4 nm, which is twice the length of the fully extended AA molecule. This implies that the molecules are tilted by less than 20° with respect to the normal to the substrate (*5*). Small-scale images were also obtained with molecular resolution (Fig. 1B). From the 2-D Fourier transform of such an image (see Fig. 2A), one may deduce the crystallographic organization of the methyl terminal groups of the aliphatic chains. This organization is hexagonal with a next neighbor distance of 5.0 ± 0.15 Å and a corresponding area per molecule of 22 ± 1 Å^2. These values were deduced from 20 images on three different samples.

In contrast to previous studies (*5*), the image size was large enough to permit accurate determination of the positional autocorrelation function (Fig. 3). The positional order correlation length (defined as the full width of the autocorrelation function) is about ten molecular spacings (50 Å). This result is comparable to the results of electron diffraction measurements performed on similar systems (*13*). This rather short-range positional order originates from the presence of defects, which can be described, as observed in Fig. 1B, as isolated or paired dislocations.

In the case of films prepared at pH = 5.5, similar results were obtained when films were observed at large scales. We found that it was never possible to obtain molecularly resolved images of those films; with the lowest force used while imaging in air (10^{-8} N), films were systematically destroyed when observed at the molecular scale. In the case of films prepared at pH = 9, we obtained exactly the same results (both at large and molecular scales) as those obtained with films prepared at pH = 6.5 (based on an examination of five different films prepared at pH = 9). Because varying pH from 5.5 to 9 increases the number of barium ions incorporated into the bilayer from 0 to a full coverage (*18*), these observations confirm the bilayer bridging role of divalent cations and show how sensitive the mechanical properties of LB films are to the presence of divalent cations.

To gain further insight, we examined the film structure as a function of heating temperature. Films prepared at pH = 6.5 and 20°C were heated for 1 hour both below (50°C) and slightly above (80°C) the bulk melting temperature of AA (74° to 76°C), under constant flow of nitrogen. Large-scale AFM images taken after the films had been cooled to 20°C (Fig. 1C) clearly show the LB film dewetting, thus leading to the formation of different types of domains coexisting with remaining patches of the initial bilayer. First we observed (for both temperatures) stacks of two to four bilayers (center of Fig. 1C), each bilayer 54 Å high. In the case of samples heated at 80°C, we also observed unlayered droplets typically 1000 Å in height (upper right corner of Fig. 1C). In some cases, stacks of two to four bilayers could be observed at the bottom of such droplets (lower right corner of Fig. 1C). In the unlayered domains, we never obtained molecularly resolved images.

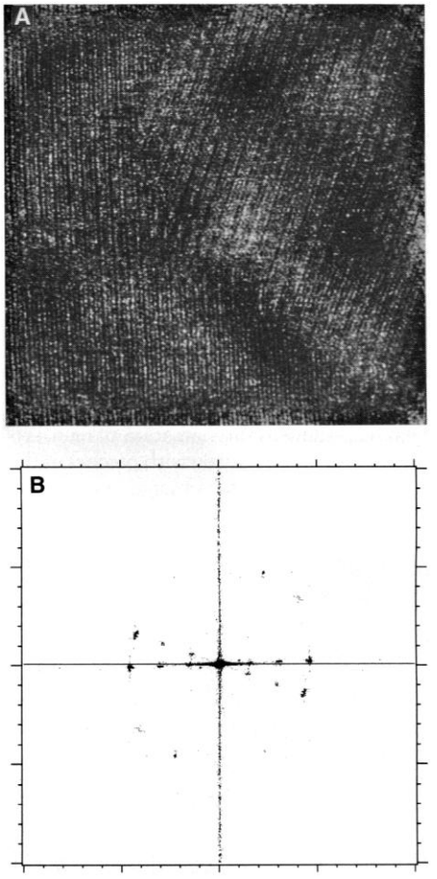

Fig. 4. AFM image of a grain boundary between two perfectly ordered regions of a barium arachidate bilayer (**A**) and the corresponding 2-D Fourier transform (**B**). In real space the size of the image is 40 nm by 40 nm. From the Fourier transform, one measures the angle between the two domains to be 20°. The peaks representative of the buckling rotate by the same amount.

The molecular organization within the patches of the remaining bilayer was found to be identical for both temperatures (Fig. 1D). The most striking feature of this image is the high degree of order within the bilayer; in this case, the correlation length is greater than 50 nm, which is the scan size compatible with the observation of the molecular structure (Fig. 3). The Fourier transform of Fig. 1D reveals a crystallographic structure (Fig. 2B) defined by the elementary basis a = 4.2 ± 0.15 Å, b = 5.0 ± 0.15 Å, γ = 64.6° ± 1°, as deduced from the analysis of 25 images on different locations of one specimen. Because these values follow the relation $a = 2b\cos\gamma$, we conclude that the lattice is a centered rectangle. The calculated area per molecule is 19.2 ± 1 Å^2. This is significantly smaller, 13%, than the area measured for unannealed samples.

Another striking feature of Fig. 2B is a

peak seen along the [10] direction of the reciprocal space whose spatial frequency corresponds to one-third of the [10] spot frequency. In direct space we observed that, perpendicular to the [10] direction, one molecular row in every three is slightly higher than the two others by about 0.2 Å (see Fig. 1D). Moreover, in the case of Fig. 1D, we observed a slight modulation of the spacing between rows perpendicular to the buckling direction. The amplitude of this modulation was estimated to be about 4% of the average row spacing. This modulation appears in the 2-D Fourier transform of Fig. 1D through the relative amplitude of the peaks along the [10] direction. Computer calculations performed on numerically defined lattices allowed us to model this 2-D Fourier transform. We were only able to simulate the relative amplitudes of the peaks along the [10] direction by taking into account at the same time a modulation of row height and a slight modulation of row spacing. Whereas the height modulation was observed systematically over the whole sample, the very subtle changes of row spacings were found to vary from one location to another on the sample. The molecular organization described above, in the case of the remaining bilayer, is found for any layer of the layered domains.

In order to rule out any artifact, we show in Fig. 4A a grain boundary observed within the same sample (*19, 20*). On each side of the boundary we observed two domains with exactly the same structure (a modulated, centered rectangular lattice) rotated by an angle of 20° (see Fig. 4B). Furthermore, such a structure was never observed on substrates (annealed or not silanated silicon wafers). We conclude that this modulation is an intrinsic crystallographic property of the annealed LB films.

From these observations, we conclude that the disordered hexagonal structure observed for unannealed samples is a metastable state. The previously measured extent of the positional order in unannealed systems is obviously related to the presence of dislocations that perturb this positional order. Those defects probably originate from constraints during the transfer of the monolayer on water onto the solid substrate. These conclusions are strongly favored by our observations that the molecular structure is not affected by the number of incorporated cations. Upon annealing, the LB films reorganize into a more ordered state of higher density, in which the area per AA molecule is almost identical to the one measured in the AA monolayer on water. The dewetting [the mechanism of which has yet to be elucidated (*21, 22*)] and the three-dimensional reconstruction of the LB film observed at macroscopic scales originate from the relaxation of internal stresses attributable to surface energy; this relaxation is responsible for the observed modulation of the molecular structure and could be due to a buckling phenomenon constrained by the LB film lattice.

REFERENCES AND NOTES

1. K B. Blodgett and I. Langmuir, *Phys Rev* **55**, 19 (1937)
2. M. Sugi, *J. Mol. Electron.* **1**, 3 (1985)
3. G. Khanarian, *Thin Solid Films* **152**, 265 (1987)
4. W. M. Reichert, C. J Bruckner, J Joseph, *ibid*, p 345.
5. L. Bourdieu, P. Silberzan, D Chatenay, *Phys. Rev. Lett.* **67**, 2029 (1991).
6. J A N. Zasadzinski *et al.*, *Biophys. J* **59**, 755 (1991).
7. H. G. Hansma *et al.*, *Langmuir* **7**, 1051 (1991)
8. E Meyer *et al.*, *Nature* **349**, 398 (1991)
9. J P K Peltonen *et al*, *J Am Chem. Soc.* **114**, 7637 (1992).
10. M. Seul, P. M. Eisenberger, H. M McConnell, *Proc. Natl. Acad. Sci. U S A.* **80**, 5795 (1983).
11. M. L. Schlossmann *et al.*, *Phys. Rev Lett* **66**, 1599 (1991).
12. K. Kjaer, E. E. Mitchell, I. R. Peterson, *Thin Solid Films* **205**, 124 (1991).
13. S Garoff, H W Deckmann, J H Dansmuir, M. S. Alvarez, *J Phys. (Paris)* **47**, 701 (1958).
14. R. Steitz, E E Mitchell, I. R Peterson, *Thin Solid Films* **205**, 124 (1991).
15. A Fisher and E. Sackmann, *J Colloid Interface Sci.* **112**, 1 (1986)
16. P Silberzan, L Léger, D. Ausserré, J J. Benattar, *Langmuir* **7**, 1674 (1991).
17. J Daillant, J. J Benattar, L. Léger, *Phys. Rev. A* **41**, 1963 (1990).
18. C Vogel *et al.*, *J. Chim. Phys Phys. Chim. Biol.* **77** (no. 10), 947 (1980).
19. P Tippmann-Krayer, H Mohwald, Yu M. L'vov, *Langmuir* **7**, 2298 (1991)
20. J Garnaes, D. K. Schwartz, R Viswanathan, J A. N. Zasadzinski, *Nature* **357**, 54 (1992)
21. F Brochard Wyart and J Daillant, *Can. J. Phys.* **68**, 1084 (1990)
22. G. Reiter, *Phys. Rev Lett* **68**, 75 (1992).

23. This work was supported by CNRS (GDR 912 "Films moléculaires flexibles" and GDR 936 "Forces de surface"). We have benefited from insightful comments from J. Prost, J. Meunier, V. Croquette, M. Goldman, and B Factor

25 September 1992, accepted 30 November 1992

Mediation of Sulfur Speciation by a Black Sea Facultative Anaerobe

K. A. Perry, J. E. Kostka, G. W. Luther III, K. H. Nealson

Shewanella putrefaciens, a respiratory facultative anaerobe isolated from the Black Sea, can reduce thiosulfate, sulfite, and elemental sulfur to sulfide readily and quantitatively. This widespread and anaerobically versatile microorganism, which is incapable of reducing sulfate, uses oxidized sulfur intermediates as electron acceptors during the respiratory oxidation of organic matter. Because of its widespread distribution and abundance, it may play a significant role in sulfur and trace metal cycling in the Black Sea and in other marine and freshwater anaerobic environments.

Recent studies have shown sulfur intermediates to be integral to electron flow between oxic and anoxic environments (*1*), although most microbiological studies involving the marine sulfur cycle have concentrated on sulfate (SO_4^{2-}) reduction or the oxidation of sulfur intermediates. *Shewanella putrefaciens* is a facultative anaerobe found in oxic, suboxic, and anoxic water columns and sediments. It is capable of utilizing a number of electron acceptors including O_2, Mn(IV), Fe(III), NO_3^-, NO_2^-, and a variety of sulfur compounds (*2, 3*). However, it cannot reduce SO_4^{2-}. To examine the contribution of this bacterium to the sulfur cycle, we grew a strain of *S. putrefaciens* isolated from the Black Sea (MR-4) anaerobically in pure culture with one of the following electron acceptors: thiosulfate ($S_2O_3^{2-}$), sulfite (SO_3^{2-}), or zerovalent sulfur (S^0) (*4*). We measured the inorganic sulfur species SO_3^{2-}, $S_2O_3^{2-}$, particulate S^0, and sulfide (HS^-) (*5, 6*) and cell density (*7*) for up to 140 hours after inoculation.

In all cultures, the electron acceptor was the only detectable sulfur species at time zero, and the decrease in its concentration with time corresponded with an increase in both HS^- and cell density (Figs. 1 to 3). The reduction of $S_2O_3^{2-}$ appeared to involve initial disproportionation of the molecule, as evinced by the appearance of SO_3^{2-} in early stages of the culture. Concentrations of SO_3^{2-} reached a maximum at 10 to 12 hours after inoculation in all replicates (Fig. 1), indicating that the bacteria first disproportionated the $S_2O_3^{2-}$ either to S^0 and SO_3^{2-} (Table 1, reaction 1), or to HS^- and SO_3^{2-} (Table 1, reaction 2), or with an electron donor such as lactate (Table 1, reaction 3). The SO_3^{2-} and S^0 (if formed) were then reduced to HS^-. All of these reactions are thermodynamically unfavorable and must be coupled to exergonic reactions such as carbon oxidation. Our data do not indicate conclusively

K A Perry, J E Kostka, G W. Luther III, College of Marine Studies, University of Delaware, Lewes, DE 19958.

K H Nealson, Center for Great Lakes Studies, University of Wisconsin, Milwaukee, WI 53204.